GSA Data Repository 2017281

Magmatic-tectonic conditions for hydrothermal venting on an ultraslow-spread oceanic core complex

J.L. Harding[1*], H.J.A. Van Avendonk[1], N.W. Hayman[1], I. Grevemeyer[2], C. Peirce[3], A. Dannowski[2]

correspondence to: jharding@utexas.edu

This PDF file includes:

Methods

Figs DR1 to DR10

Table DR1

2017281_Database DR1_oceanic crustal thickness data.xlsx

Methods

Na8.0 Compilation

The concentrations of incompatible element Na were compiled from basalts at different spreading segments around the globe with different spreading rates (Gale et al., 2014). Na8.0 values are normalized to a MgO wt % of 8.0 using liquid-line of descent models (Klein & Langmuir, 1987). Na8.0 values from locations close to hot spot influence, in particular the Afar, Iceland and Samoa hotspots. These values are plotted vs. segment spreading rate as a red cloud (Fig. DR1), as well as data points with error bars are plotted (Fig DR2).

Oceanic Crustal Thickness Compilation

Oceanic crustal thicknesses determined from over 200 seismic refraction studies were compiled with spreading rate and seafloor age extracted for each data point using isochrones (Müller et al., 2008) (see Database DR1). Data points were excluded from the compilation if they were influenced by hot spots or fracture zones. Crustal thickness vs. spreading rate is plotted as a blue cloud (Fig. DR1) and as data points with error bars (Fig. DR3), excluding data collected before 1970 and from seafloor older than 20 Ma.

Seismic Tomography

We used active-source ocean-bottom seismometer (OBS) data collected along Line 2 (Fig. 1) during the CaySeis cruise to produce the P-wave seismic velocity image (Fig. 2). An airgun array of 12 G-guns with a total volume of 84 liters was towed behind the *F/S Meteor*, producing seismic energy that was recorded by OBSs on the seafloor

between 4 to 20 Hz. These OBSs were pooled from three institutions, the University of Texas Institute for Geophysics in Austin, Texas, the NERC's Ocean-Bottom Instrumentation Facility in the UK, and the GEOMAR Centre for Ocean Research in Kiel, Germany. OBSs were spaced ~ 5 km apart along the seafloor, with shots every minute (~ 150 m shot spacing). A total of 18 OBSs comprise Line 2.

P-wave first arrival times were first picked from the wide-angle refraction data collected by each OBS (Fig. DR4). Phases were not distinguished due to the rough bathymetry and complicated structure of the Mid-Cayman Spreading Center (MCSC). These picked times were assigned an error from 50 to 200 ms based on signal to noise ratio and offset. These times were then inverted for P-wave velocities throughout a 106 x 25 km model space (Van Avendonk at al., 1998*;* Van Avendonk et al., 2001). Additionally, multiple refractions were picked and incorporated into the inversion in order to improve imaging of distal areas of the model space. These multiples represent P-wave refractions with an additional bounce in the water column above the OBS.

The tomographic inversion process begins with a starting seismic velocity model based on assumptions of oceanic crustal velocity structure (Fig. DR5). The raypaths from all source-receiver pairs were calculated through the starting model using a hybrid shortest path and raybending method (Van Avendonk et al., 2001) in a 3D (extended ±1.6 km perpendicular to Line 2) model space to account for the rough bathymetry. The difference between the picked P-wave travel times and calculated travel times are then inverted for seismic velocities everywhere in the model space using a linearized least-squares approach (Van Avendonk at al., 1998*;* Van Avendonk et al., 2001). This process of calculating raypaths in the new model and then producing a new velocity model with a

least squares inversion is repeated until a minimum data misfit is achieved. In 9 iterations, the residual mean data fit reduced from 672 ms to 95 ms and the chi-squared reduced from 44.53 to 0.67.

The iterative nonlinear tomographic inversion converged on two solutions that both achieve a good data fit. These two solutions differ in the nature of the low-velocity zone beneath Mt. Dent, to which the raypaths appear to be sensitive. To account for this, we averaged 12 seismic velocity models from consecutive iterations of the inversion passed the 9^{th} iteration that produced an acceptable data misfit. This average represents our final, preferred velocity model, with a residual mean data misfit of 95 ms and a chi-squared of 0.67. Fig. DR6 shows the final seismic tomographic image with picked and calculated travel times. The standard deviation of the final model (using the 12 inversion results) was calculated (Fig. DR7). A resolution test was also carried out in order to show how well the final velocity model resolves a body that is 10 km-wide by 5 km-high (Fig. DR8). Table S1 summarizes the errors for all 18 OBSs.

Gravity

The shipboard gravity data were corrected to the Free-air Anomaly (FAA) (Fig. DR10, middle panel). This FAA was then modeled for density in the center portion of Line 2 where seismic control is best. Starting with velocity contours from the velocity model, four layers were defined: a water layer, an upper crustal layer, a lower crustal layer, and an upper mantle layer. These layers were then assigned densities and then forward modeled to match the FAA (Fig. DR10, bottom panel). The water layer has a density of 1.03 g cm^{-3}, the upper crustal layer has a density of 2.55 g cm^{-3}, the lower

crustal layer has a density of 2.65 g cm^{-3}, and the upper mantle layer has a density of 3.33 g cm^{-3}. This modelling shows that Mt. Dent has relatively lower densities than the surrounding lithosphere to the east and west.

Magnetics

The summit of Mt. Dent is ~14 km east of the center of the MCSC, ~2 my of spreading judging by the long-term ~7.5 mm/yr half-rate, based primarily on magnetic anomaly 3A, 5A and 6, all in off-axis crust >5 Ma-old (Leroy et al., 2000). The protracted evolution of the Mt. Dent OCC is indicated by the edge of the central magnetic anomaly along its eastern edge and an older positive magnetic anomaly along its western edge (Fig. DR10, top panel) (Hayman et al., 2011). The ultraslow spreading rate renders the exact ages of these anomalies unclear, but we take the older edge of the central anomaly to be ~0.71 Ma and the youngest age of the next oldest positive anomaly to be the edge of anomaly 2A, ~3.3 Ma (Leroy et al., 2000).

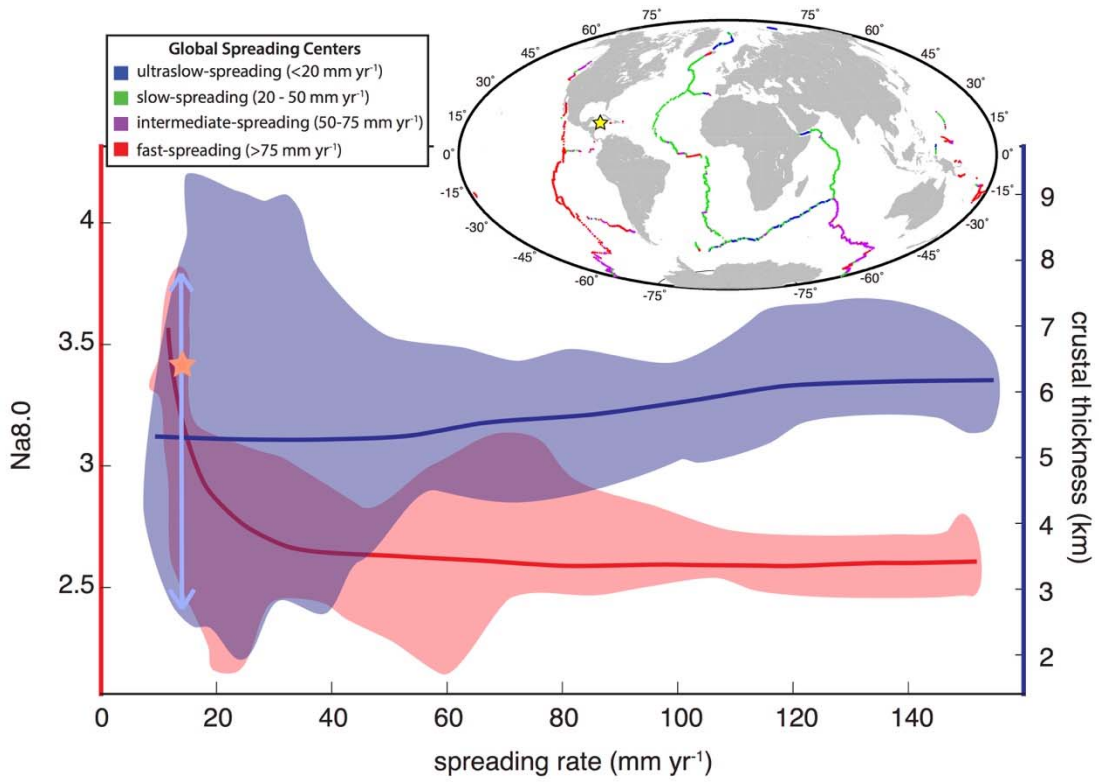

Fig. DR1:

Left-hand Y-axis is Na8.0 for segments of different spreading rate, incompatible element Na normalized to an MgO of 8.0 Wt. % in liquid-line-of descent models (Gale et al., 2014). Inset shows the location of the Mid-Cayman Spreading Center (MCSC) (yellow star) and several other ultraslow spreading systems in a global view. Crustal thickness values (right-hand Y-axis) are from a new compilation of seismic refraction studies conducted in the last 40 years. The plot illustrates that at spreading centers far from mantle plumes, incompatible elements become enriched and crustal thickness becomes more variable as a result of low extents of mantle melting when spreading rate drops to < 20 mm yr^{-1} (Dalton et al., 2014). The MCSC is important in this compilation because it has some of the highest Na8.0 concentrations (red star), and previously reported lowest crustal thickness values; as we show here the MCSC has highly variable crustal thickness over time (light blue line) (Fig. DR3).

1

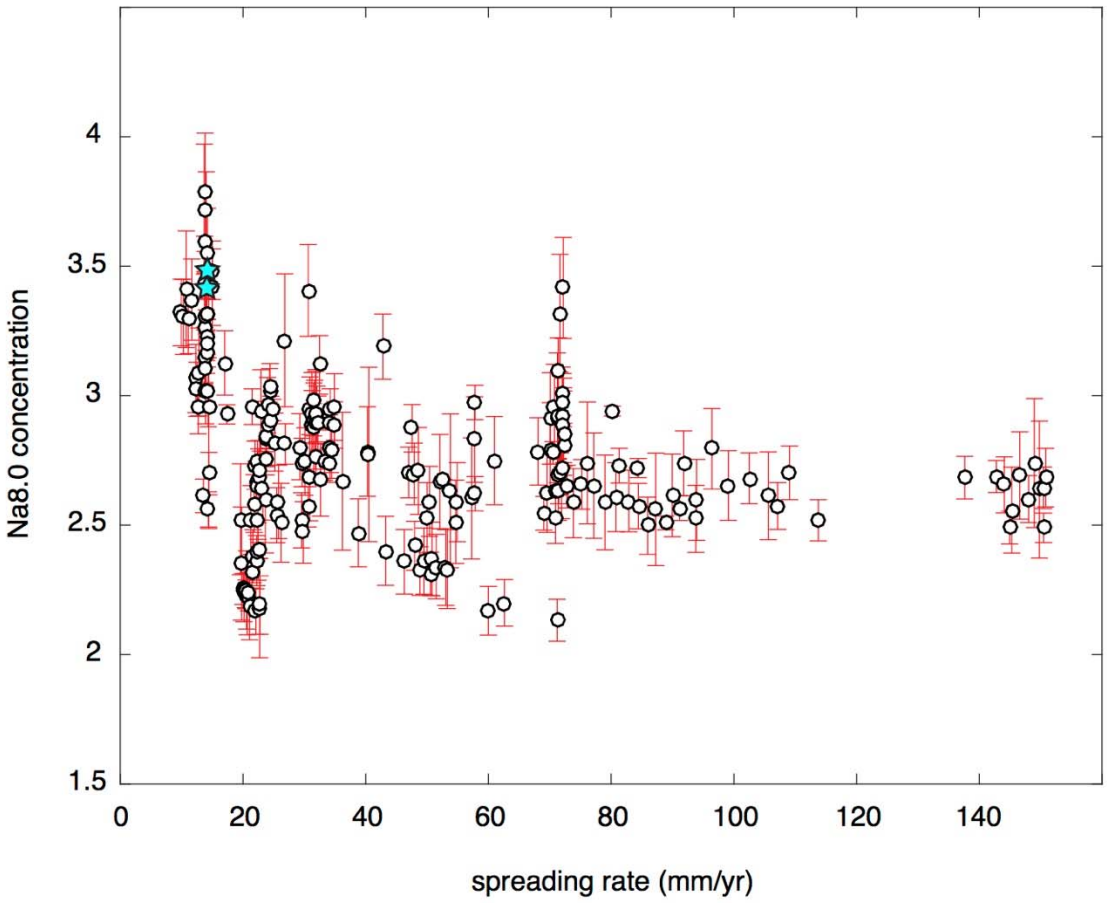

Fig. DR2

Na8.0 of basalts from segments of different spreading rates, where Na is normalized to an MgO of 8.0 Wt. % in liquid-line-of descent models (Gale et al., 2014). Data near hotspots were excluded from this plot. Mid-Cayman Spreading Center (MCSC) data is denoted by the cyan stars. At spreading rates slower than ~ 20 mm yr^{-1}, Na8.0 concentrations sharply increase, suggesting less mantle melting at ultraslow-spreading centers such as the MCSC.

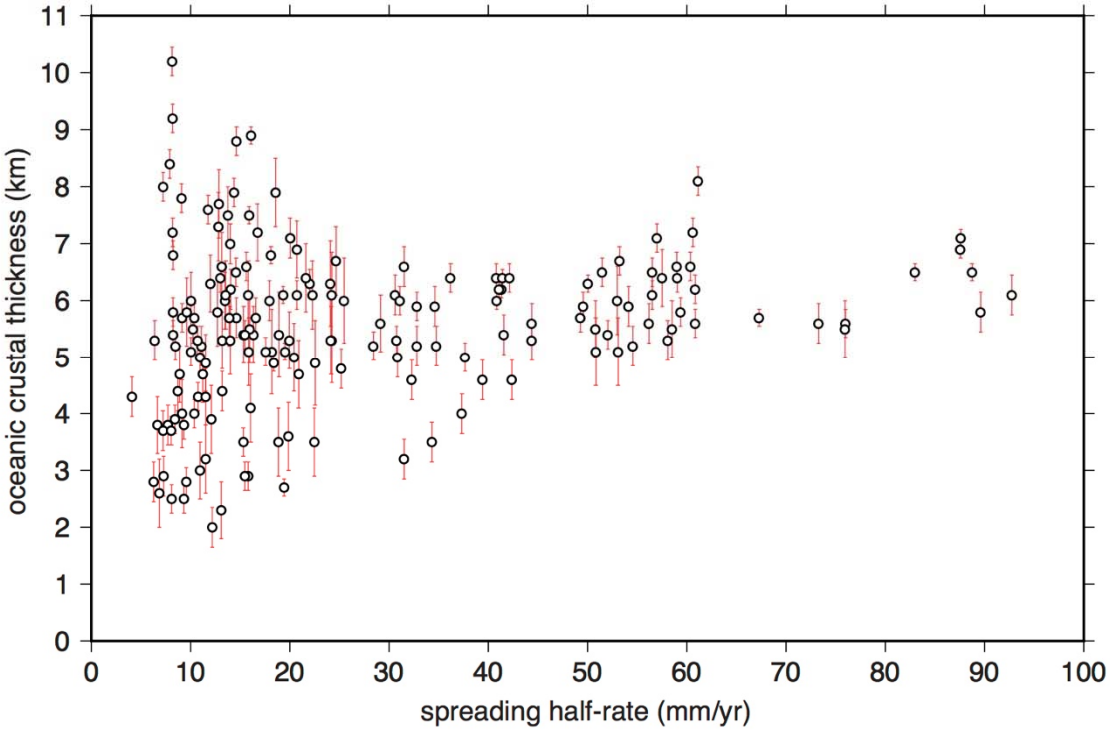

Fig. DR3

Oceanic crustal thickness vs. spreading half-rate from a compilation of seismically-determined oceanic crustal thicknesses. Crustal thickness estimates included are of oceanic crust younger than 20 Ma, collected since 1970, and away from hot spots or fracture zones. This database is included as a separate file (Database DR1). Oceanic crustal thickness averages ~ 6.0 km for spreading half-rates above 50 mm yr^{-1}, with crustal thickness decreasing slightly for slower spreading rates. A significant change in variability of crustal thickness can be observed at spreading half-rates lower than 50 mm yr^{-1}, showing that ultraslow-spreading centers like the Mid-Cayman Spreading Center behave differently from faster spreading centers.

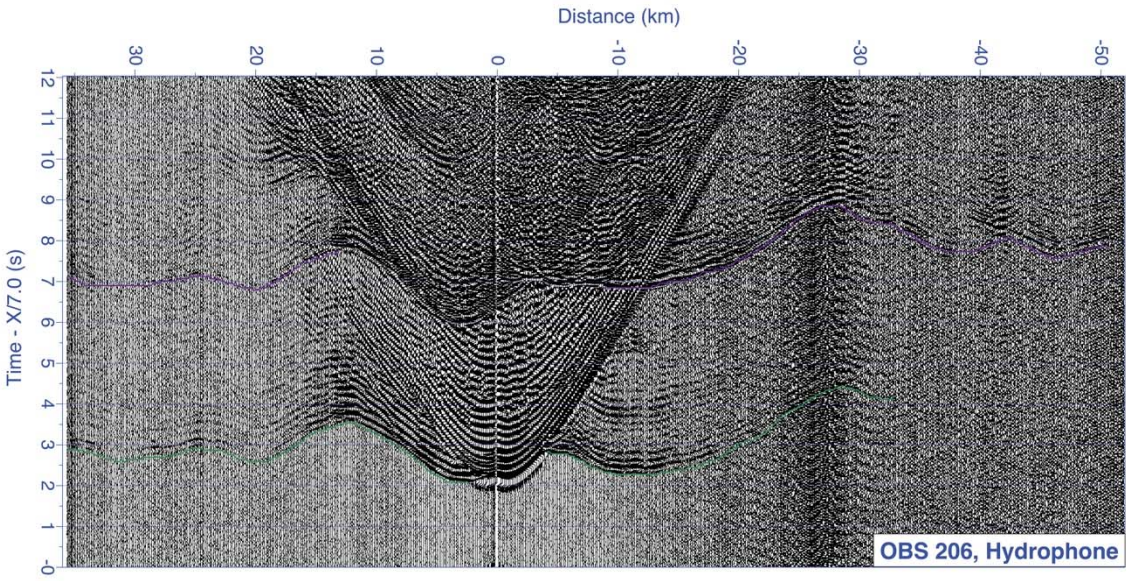

Fig. DR4

Wide-angle refraction data from the hydrophone channel of OBS 206, plotted as time at a reduction velocity of 7 km s^{-1}, and band-pass filtered between 5-15 Hz. The first-arrival P-wave travel-time picks are shown as green lines and the multiple P-wave picks are shown as purple lines.

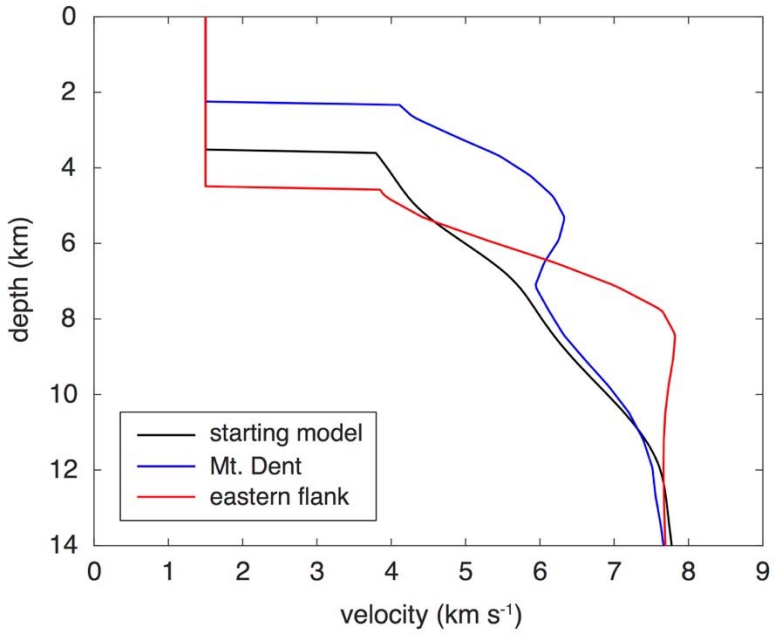

Fig. DR5

Velocity-depth profiles of the starting velocity model (black), Mt. Dent (red), and the eastern flank (blue), which correspond to the dotted lines in the bottom panel of Fig. 2.

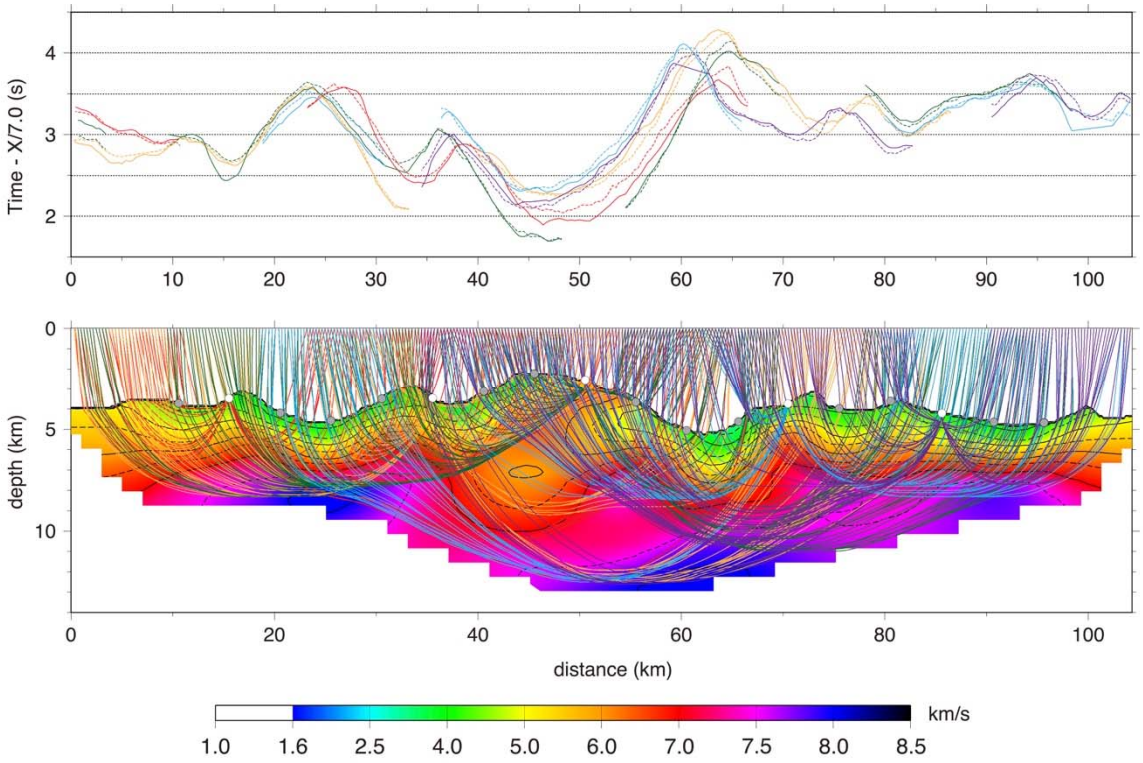

Fig. DR6

Raytracing diagram for the final seismic velocity model for Line 2. Top panel shows the picked (solid lines) and calculated (dashed lines) P-wave travel times, including multiples, plotted at a reduction velocity of 7 km s^{-1}, along Line 2. Colors indicate different OBSs that recorded these arrivals, which correspond to the bottom panel. The bottom panel shows the final seismic velocity model at 2x vertical exaggeration with raypaths for six different OBSs: 202 (red), 206 (orange), 209 (green), 213 (cyan), and 216 (purple).

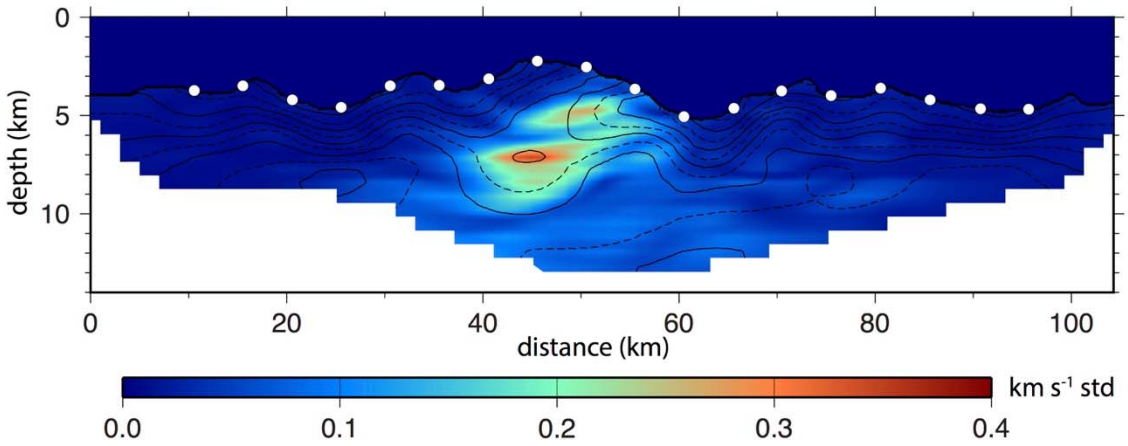

Fig. DR7

Standard deviation of the final seismic tomographic model at 2x vertical exaggeration. White circles are OBS locations. Standard deviations range from 0 to 0.4 km $s^{-1.}$ Most standard deviations are < 0.1 km s^{-1}, showing that the final model is stable; differences below Mt. Dent arise from the sensitivity of raypaths near the low velocity zone.

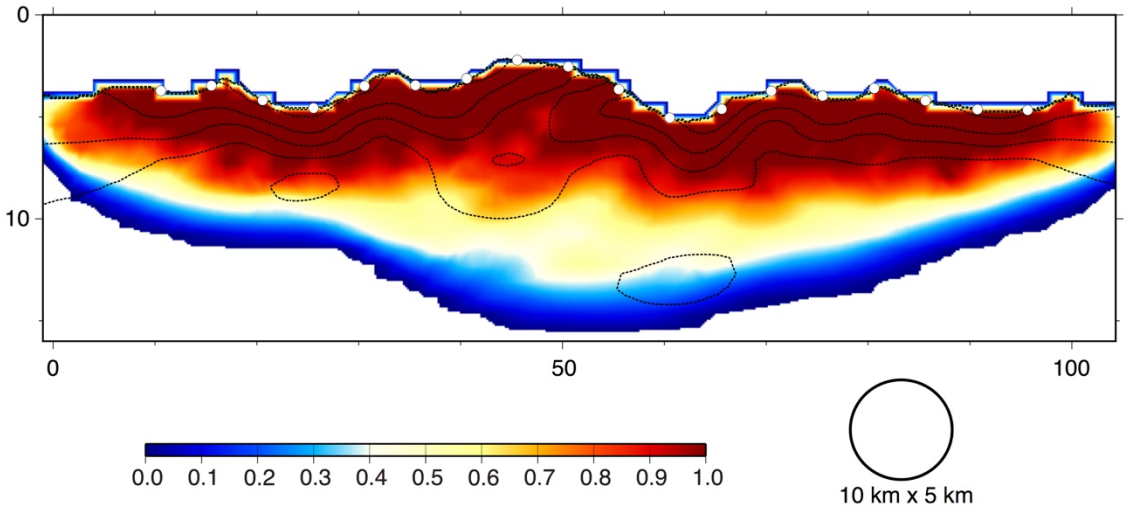

Fig. DR8

Line 2 resolution test for a 10 km-wide and 5 km-high body, plotted at 2x vertical exaggeration. A value of 1 (red) indicates full resolution of a body this size and a value of 0 (blue) means a body of this size cannot be resolved. OBSs are shown as white circles.

Table DR1:

OBS	Number of picks	Mean of travel-time residual (ms)	RMS misfit (ms)	Chi-squared
201	194	-24	78	0.583
202	168	-61	101	0.519
203	246	5	69	0.298
204	229	-5	58	0.424
205	183	-7	102	0.789
206	258	23	70	0.413
207	287	-69	88	0.735
208	218	-54	91	0.750
209	250	-8	88	0.628
210	143	145	198	3.017
211	295	7	58	0.370
212	255	101	151	0.831
213	202	-39	83	0.497
214	287	13	101	0.568
215	238	-37	74	0.583
216	201	8	79	0.959
217	185	29	89	0.472
218	73	76	108	0.586

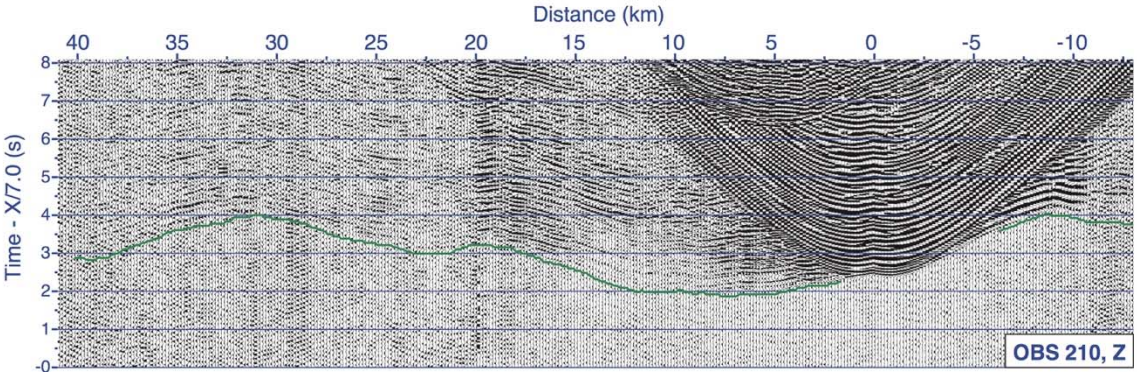

Fig. DR9

Wide-angle refraction data from the Z channel of OBS 210, plotted as time at a reduction velocity of 7 km s^{-1}, and band-pass filtered between 5-15 Hz. The first-arrival P-wave travel-time picks are shown as green lines and no multiple P-wave were picked for this instrument.

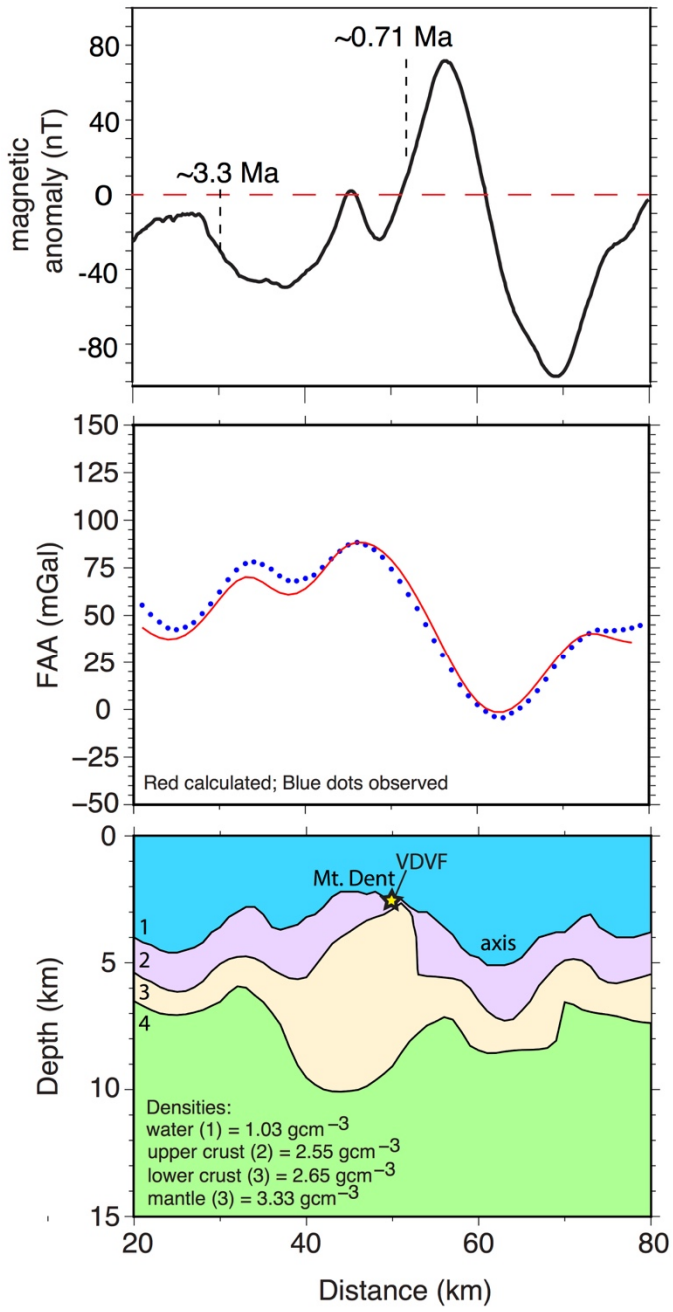

Fig. DR10

Top panel shows the shipboard gravity from Line 2, and the magnetic anomalies over the Mt. Dent detachment fault labeled with approximate reversal ages (Hayman et al., 2011). Middle panel shows the Free-air Anomaly (FAA) (blue dots) compared with the calculated FAA from density modelling (red line). Bottom panel shows the density model

to produce the calculated FAA. The density model consists of (1) a water layer of density 1.03 g cm $^{-3}$, (2) an upper crustal layer of density 2.55 g cm^{-3}, (3) a lower crustal layer of density 2.65 g cm^{-3}, and (4) an upper mantle layer of density 3.33 g cm^{-3}. The gravity modelling shows that Mt. Dent has lower-crustal densities with a deep crustal root.

ADDITIONAL REFERENCES:

Leroy, S., Mauffret, A., Patriat, P., and Mercier de Lepinay, B., 2000, An alternative interpretation of the Cayman trough evolution from a reidentification of magnetic anomalies: Geophysical Journal International, v. 141, p. 539-557. doi:10.1046/j.1365-246x.2000.00059.x

Müller, R.D., Sdrolias, M., Gaina, C., and Roest, W.R., 2008, Age, spreading rates, and spreading asymmetry of the world's ocean crust: Geochemistry, Geophysics, Geosystems, v. 9, no.4, doi:10.1029/2007/gc001743.